Monthly Notices
of the
ROYAL ASTRONOMICAL SOCIETY

Mon. Not. R. Astron. Soc. **403,** 2063–2076 (2010) doi:10.1111/j.1365-2966.2010.16256.x

X-ray groups and clusters of galaxies in the Subaru–XMM Deep Field

A. Finoguenov,[1,2⋆] M. G. Watson,[3] M. Tanaka,[4] C. Simpson,[5] M. Cirasuolo,[6] J. S. Dunlop,[6] J. A. Peacock,[6] D. Farrah,[7] M. Akiyama,[8] Y. Ueda,[9] V. Smolčić,[10] G. Stewart,[3] S. Rawlings,[11] C. van Breukelen,[11] O. Almaini,[12] L. Clewley,[11] D. G. Bonfield,[13] M. J. Jarvis,[13] J. M. Barr,[11] S. Foucaud,[12] R. J. McLure,[6] K. Sekiguchi[14] and E. Egami[15]

[1]*Max-Planck-Institut für extraterrestrische Physik, Giessenbachstraße, 85748 Garching, Germany*
[2]*University of Maryland, Baltimore County, 1000 Hilltop Circle, Baltimore, MD 21250, USA*
[3]*X-ray Astronomy Group, Department of Physics and Astronomy, University of Leicester, Leicester LE1 7RH*
[4]*European Southern Observatory, Karl-Schwarzschild-Str 2, 85748, Garching, Germany*
[5]*Astrophysics Research Institute, Liverpool John Moores University, Twelve Quays House, Egerton Wharf, Birkenhead CH41 1LD*
[6]*Scottish Universities Physics Alliance, Institute for Astronomy, University of Edinburgh, Royal Observatory, Edinburgh EH9 3HJ*
[7]*Department of Physics & Astronomy, University of Sussex, Falmer, Brighton BN1 9RH*
[8]*Astronomical Institute, Tohoku University, Sendai 980-8578, Japan*
[9]*Department of Astronomy, Kyoto University, Kyoto 606-8502, Japan*
[10]*California Institute of Technology, MC 105-24, 1200 East California Boulevard, Pasadena, CA 91125, USA*
[11]*Astrophysics, Department of Physics, Keble Road, Oxford OX1 3RH*
[12]*School of Physics and Astronomy, University of Nottingham, University Park, Nottingham NG7 2RD*
[13]*Centre for Astrophysics Research, Science & Technology Research Institute, University of Hertfordshire, Hatfield AL10 9AB*
[14]*Subaru Telescope, National Astronomical Observatory of Japan, 650 N. A'ohoku Place, Hilo, Hawaii 96720, USA*
[15]*Steward Observatory, University of Arizona, 933 N. Cherry Ave., Tucson, AZ 85721, USA*

Accepted 2009 December 22. Received 2009 December 18; in original form 2009 September 24

ABSTRACT

We present the results of a search for galaxy clusters in the Subaru–XMM Deep Field (SXDF). We reach a depth for a total cluster flux in the 0.5–2 keV band of 2×10^{-15} erg cm^{-2} s^{-1} over one of the widest *XMM–Newton* contiguous raster surveys, covering an area of 1.3 deg^2. Cluster candidates are identified through a wavelet detection of extended X-ray emission. The red-sequence technique allows us to identify 57 cluster candidates. We report on the progress with the cluster spectroscopic follow-up and derive their properties based on the X-ray luminosity and cluster scaling relations. In addition, three sources are identified as X-ray counterparts of radio lobes, and in three further sources, an X-ray counterpart of the radio lobes provides a significant fraction of the total flux of the source. In the area covered by near-infrared data, our identification success rate achieves 86 per cent. We detect a number of radio galaxies within our groups, and for a luminosity-limited sample of radio galaxies we compute halo occupation statistics using a marked cluster mass function. We compare the cluster detection statistics in the SXDF with that in the literature and provide the modelling using the concordance cosmology combined with current knowledge of the X-ray cluster properties. The joint cluster $\log(N) - \log(S)$ is overpredicted by the model, and an agreement can be achieved through a reduction of the concordance σ_8 value by 5 per cent. Having considered the $\mathrm{d}n/\mathrm{d}z$ and the X-ray luminosity function of clusters, we conclude that to pin down the origin of disagreement a much wider (50 deg^2) survey is needed.

Key words: surveys – cosmology: observations – dark matter – large-scale structure of Universe.

1 INTRODUCTION

Extended X-ray emission from groups and clusters of galaxies is an unambiguous signal of high-density and high-mass environments (e.g. Borgani & Guzzo 2001; Rosati, Borgani & Norman 2002).

⋆E-mail: alexis@mpe.mpg.de

© 2010 The Authors. Journal compilation © 2010 RAS

The low scatter of X-ray emission around the mean with respect to the underlying mass of the object and advances in X-ray surveys have established X-rays as one of the most reliable tools in the search of massive haloes (e.g. Böhringer et al. 2002). Deep *XMM* and *Chandra* surveys such as Chandra Deep Field South (CDFS; Giacconi et al. 2002), Chandra Deep Field North (CDFN; Bauer et al. 2002), Lockman Hole (Finoguenov et al. 2005), the Cosmic Evolution Survey (COSMOS; Finoguenov et al. 2007), XMM-Large Scale Structure (LSS) (Pacaud et al. 2007), the Canadian Network for Observational Cosmology (CNOC2; Finoguenov et al. 2009) show the potential of efficient group/cluster detection and illustrate their competitiveness with spectroscopic group surveys. Such data have contributed directly to studies of galaxy formation (e.g. Tanaka et al. 2008; Giodini et al. 2009), LSS and its relation to active galactic nucleus (AGN) activity (Silverman et al. 2009), and also have shown the power of X-ray surveys to find and study sky densities in excess of 100 groups per square degree (Bauer et al. 2002).

At high redshifts, deep X-ray surveys both offer the highest sensitivity towards the cluster mass and are competitive to the best optical surveys for finding groups. Clusters at different redshifts provide homogeneous samples of galaxies in a high-density environment, enabling studies of the evolution of stellar populations (e.g. Blakeslee et al. 2003; Lidman et al. 2004; Mei et al. 2006; Strazzullo et al. 2006). Current results from the deep near-infrared fields indicate a strong evolution in galaxy colour segregation near redshift 1.7 (Cirasuolo et al. 2007). Deep X-ray surveys of the same fields are therefore of further importance to provide direct evidence of the role of groups and clusters of galaxies in cosmic galaxy build up.

This paper concentrates on cataloguing and analysis of the statistical properties of the X-ray clusters primarily detected in *XMM* observations of the Subaru–XMM Deep Field (SXDF). The basic X-ray data reduction and a construction of the catalogue of extended sources are discussed in Section 2. In Section 3, we describe the cluster identification using a refined red-sequence method by including a galaxy pre-selection using a multiband photometric redshift catalogue. The spectroscopic follow-up is presented in Section 4. In Section 5, we provide a final catalogue of identified clusters, including the results of the spectroscopic follow-up. This is the first X-ray survey where special care is taken to select out the systems where extended X-ray emission is caused by radio lobes. The details and the results of this procedure are outlined in Section 5.1. Statistical properties of the clean X-ray cluster sample are discussed at the end of Section 5. Section 6 concludes the paper.

All through this paper, we adopt a 'concordance' cosmological model, with $H_0 = 72\,\mathrm{km\,s^{-1}\,Mpc^{-1}}$, $\Omega_\mathrm{M} = 0.25$, $\Omega_\Lambda = 0.75$ (Komatsu et al. 2009), and – unless specified – quote all X-ray fluxes in the [0.5–2] keV band and rest-frame luminosities in the [0.1–2.4] keV band and provide confidence intervals at the 68 per cent level.

2 *XMM* DATA REDUCTION

The SXDF incorporates a deep, large-area X-ray mosaic with *XMM–Newton*, consisting of seven overlapping pointings covering a $1.3\,\square^\circ$ region of the high Galactic latitude sky with an exposure time of 100 ks in the central field (in separate exposures) and 50 ks in the flanking fields (for details see Geach et al. 2007). Four of the pointings were carried out in 2000 August, and the remaining three were made in 2002 August and 2003 January.

For the cluster detection, we used the *XMM–Newton* mosaic image in the 0.5–2 keV band, consisting of seven pointings, 400 ks in total. A description of the *XMM–Newton* observatory is given by Jansen et al. (2001). In this paper, we use the data collected by the European Photon Imaging Cameras (EPIC): the *pn*-CCD camera (Strüder et al. 2001) and the MOS-CCD cameras (Turner et al. 2001). All EPIC-*pn* observations have been performed using the Thin filter, while both EPIC-MOS cameras used the Medium filter.

In addition to the standard data processing of the EPIC data, which was done using XMMSAS version 6.5 (Watson et al. 2001; Kirsch et al. 2004; Saxton et al. 2005), we perform a more conservative removal of time intervals affected by solar flares, following the procedure described in Zhang et al. (2004). In order to increase our capability of detecting extended, low surface brightness features, we have applied the 'quadruple background subtraction' (Finoguenov et al. 2007) and also check for high background that can be present in a few MOS chips (Snowden et al. 2008), identifying none. The resulting countrate-to-flux conversion in the 0.5–2 keV band excluding the lines is 1.59×10^{-12} for *pn* and 5.41×10^{-12} for each MOS detector, calculated for the source spectrum, corresponding to the Astrophysical Plasma Emission Code (APEC; Smith et al. 2001) model for a collisional plasma of 2 keV temperature, 1/3 solar abundance and a redshift of 0.2. We note that in reconstructing the properties of the identified groups and clusters of galaxies, we implement the exact corrections, based on the source spectral shape (as defined by the expected temperature of the emission) and the measured redshift of the system.

After the background has been estimated for each observation and each instrument separately, we produce the final mosaic of cleaned images and correct it for the mosaic of the exposure maps in which we account for differences in sensitivity between *pn* and MOS detectors.

We use the prescription of Finoguenov et al. (2009) for extended source detection, which consists of removal of the point spread function (PSF) model for each detected point source from the data before applying the extended source search algorithm. The signal-to-noise ratio image of the point-source cleaned image is shown in Fig. 1. As can be seen from the figure, the image exhibits a fairly uniform signal-to-noise ratio. Without the refined background subtraction, the signal-to-noise image exhibited large-scale variations, which could mimic an extended source. On the image, the ellipses show the position and the angular extent of detected sources. The total number of extended sources detected is 84. Identification of sources is required to split several sources, increasing the total to 92. The threshold for the wavelet source detection has been set to four standard deviations. The calibrated map of the wavelet noise (Vikhlinin et al. 1998) has been produced and used for modelling of the survey sensitivity. The extent of the source, which we used for identification and flux estimates, has been followed down to 1.6 times the local wavelet noise value. The significance of the flux estimate can be lower than 4σ. This is due to a change in the significance of the source between the peak of its significance and its extent as well as a difference in the error field for detection and flux extraction. The later difference is driven by a difference in the fluctuation level between the wavelet noise (important for detection) and unsmoothed source+noise (important for the flux estimate). These differences decrease with the increasing exposure of the survey (and e.g. are gone in our analysis of CDFS; Finoguenov et al., in preparation). Apart from the allowance for systematical errors associated with AGN removal lately, the procedures of calculating the sensitivity maps are the same as in Finoguenov et al. (2007). Prior removal of point sources

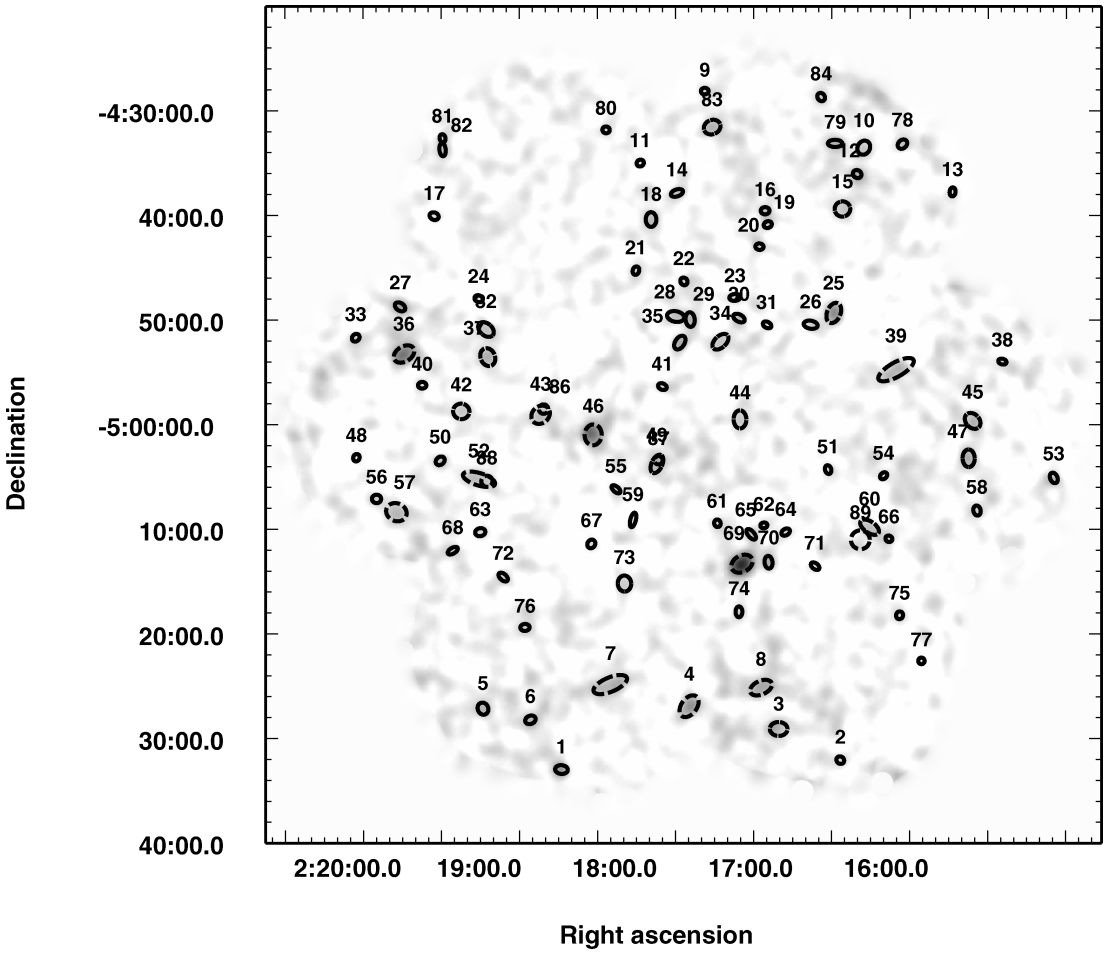

Figure 1. An image of the signal-to-noise ratio in the 0.5–2 keV band after background subtraction and point source removal. The image has been smoothed with a Gaussian of 32 arcsec width. White colour corresponds to the values smaller than 0, grey colour starts at 1σ and black colour corresponds to detection significance of 6σ per 200 square arcsecond element. Ellipses indicate the wavelet sources, labelled according to the catalogue. The coordinate grid is for the Equinox 2000.

simplifies the extended flux estimate and also allows us to use the X-ray centre of extended emission as a prior for identification, as detailed below and illustrated in Fig. 2. A small fraction of sources ($\sim$15 per cent) remains unidentified even in the area with best follow-up data. Only 6 per cent can be accounted for by remaining deficiencies with the source identification (see below). We believe this can be an effect associated with joint detection of a number of subthreshold point sources (e.g. Burenin et al. 2007). A study of the origin of this source population is on-going using CDFS and CDFN data, where one can profit from *Chandra* resolution (Finoguenov et al., in preparation).

3 REFINED RED-SEQUENCE TECHNIQUE FOR CLUSTER IDENTIFICATION

As a primary method for cluster identification we used the refined red-sequence technique, described in this section. This is a further refinement of the photo-z concentration technique, used in Finoguenov et al. (2007). Uncertainty, related to identification of clusters based on the photo-z data alone has been addressed in van Breukelen et al. (2007). We deem our technique as the most robust cluster identification when only broad-band photometric data are available. With the refinements, described here, this technique is also sensitive to identification of galaxy groups. However, strongly star-forming galaxy groups cannot be detected through such techniques. This point is thoroughly checked using the zCOSMOS survey, yielding only 1 per cent of such systems (Finoguenov et al., in preparation), which are located at $z < 0.3$. As we discuss below, our identification at $z < 0.3$ is anyway not complete, due to lack of U-band photometry.

First, we consider the calibration of the model red sequence, then we detail the application procedure and describe selection criteria. To model the evolution of the red sequence, we adopt the passive evolution model of a single stellar population (SSP), assuming no dust extinction, using the Bruzual & Charlot (2003) population synthesis code. In order to reproduce the slope of the red sequence, the red sequence in the Coma cluster (Bower, Lucey & Ellis 1992) has been fitted by the SSP models formed at $z_f = 5$ with various metallicities. Model galaxies are 'calibrated' in this way (Lidman et al. 2008). The model red sequence can then be evolved back in time to arbitrary redshifts. Note that this modelling is based on the assumption that the slope of the red sequence is entirely due to the mass–metallicity relation, as suggested both by observations and in theoretical work (e.g. Kodama & Arimoto 1997; Stanford, Eisenhardt & Dickinson 1998).

The fitting procedure is three-fold. First, we extract galaxies in the area centred on the extended X-ray emission. We then estimate significance of an overdensity of red galaxies around the model

© 2010 The Authors. Journal compilation © 2010 RAS, MNRAS **403,** 2063–2076

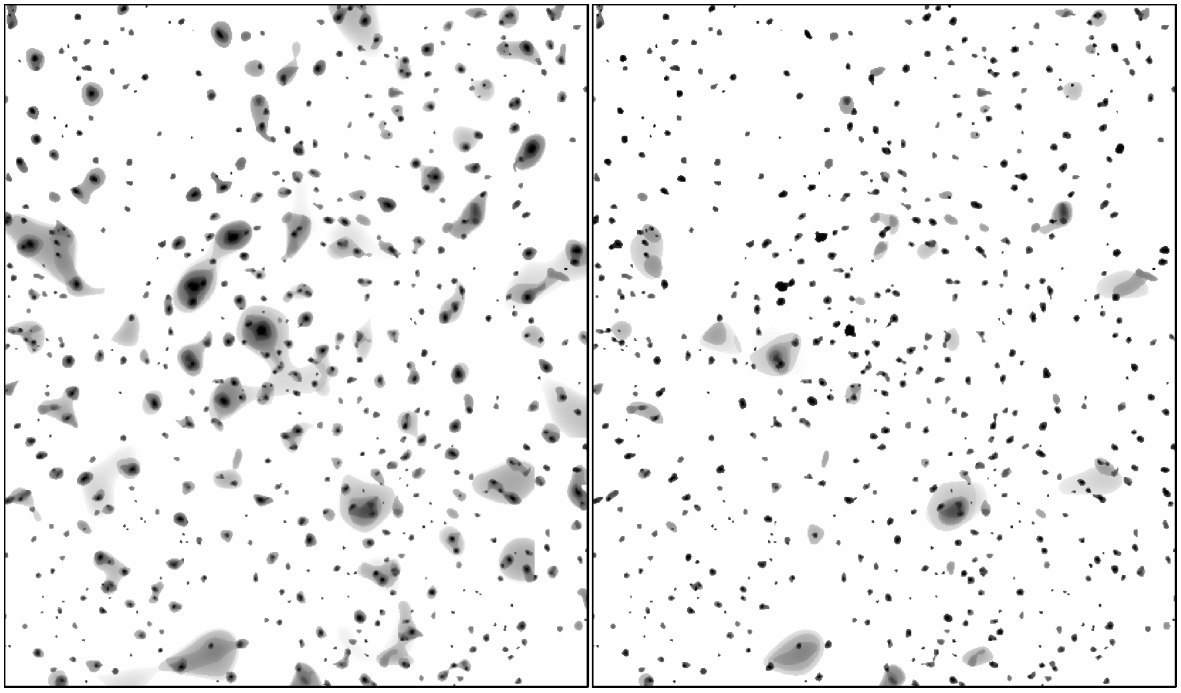

Figure 2. Comparison of two wavelet reconstructions of the SXDF field. Left-hand panel displays a standard scale-wise decomposition, right-hand panel includes a three-level subtraction of the PSF wings associated with the point-like sources, as described in the text. The scale limits for both images are the same. Clearly the left-hand panel is much less diffuse. Both images are 45×55 arcmin^2. The pixel size is 4 arcsec on a side.

red sequence at a given redshift. This procedure is performed at $0 < z < 2.5$. All significant (with details given in the following sections) detections are stored for further consideration. Next, we go through the step of approving the identifications. The results of spectroscopic follow-up of similar sources in the CNOC2 field, discussed in Finoguenov et al. (2009), showed that the most reliable identification has more than three galaxies inside the X-ray shape of the source. In using the red sequence, to avoid chance projection a small dispersion of galaxies with respect to the model red sequence will also be preferred. We therefore favour these identifications, even if they are not the most significant ones. When two or more identifications fit, we consider splitting the X-ray source according to the galaxy counterpart and check significance of these new sources, retaining only the significant ones and assigning a lower flag (=2), if such a procedure is impossible, the X-ray source is identified as confused (flag = 4). Robust identifications have a clear concentration of red galaxies inside the detected X-ray emission. Some identifications are less obvious and require more follow-up work. These are marked correspondingly (flag = 3). A comprehensive list of source flags is discussed in Section 5. Now we present the details of the method.

3.1 Construction of the photometric catalogue

We use the Subaru *BVRiz* photometric catalogue from DR1 (Foucaud et al. 2007; Furusawa et al. 2008). The z-band selected catalogue is used for this work. We also use *JHK* photometry from UKIDSS (UKIRT Infrared Deep Sky Survey) Ultra Deep Survey (UDS) third data release (DR3; Warren et al., in preparation). Objects from UDS are cross-correlated with the Subaru catalogue. The catalogue is further supplemented by *Spitzer* IRAC photometry from the deep SpUDS programme (PI James Dunlop) and the *Spitzer* Wide-area InfraRed Extragalactic survey (SWIRE; Lonsdale et al. 2003). We use SExtractor to detect objects on the IRAC images and cross-correlate the IRAC objects with the Subaru objects. We use a 2 arcsec aperture for the IRAC photometry and apply a point-source aperture correction to estimate total magnitudes. Since data from different telescopes have different PSF sizes, we use total magnitudes to derive colours. Stars are removed on the basis of their colours and compactness.

We then feed the catalogue to our photometric redshift code. A detailed description of the code is given in Tanaka et al. (2008), but a brief outline is given here. The code uses a library of templates based on Bruzual & Charlot (2003) models. We assume the τ model to describe the star formation histories of galaxies and allow τ, dust extinction and intergalactic extinction to vary. Each observed object is fitted with all the templates and the best-fitting model is determined using the χ^2 statistics. The quality of the photometric redshift estimate has been compared to the spectroscopic redshifts, yielding 10 per cent outliers ($|z_{\rm phot} - z_{\rm spec}| > 0.2$) and $0.03(1 + z)$ uncertainty on redshift estimate below $z_{\rm spec} = 4$. The dominant fraction of outliers is at $z < 0.3$ and is due to lack of U-band data.

3.2 Selection of galaxies for cluster identification

As mentioned above, we go over the redshift (z) at which we apply the cluster red-sequence method. We select galaxies at $|z - z_{\rm phot}| < 0.2$, where $z_{\rm phot}$ is a photometric redshift. Next, we only consider the galaxies located within 0.5 Mpc (physical) from the centre of X-ray emission at a given redshift (see description of equation 1 below for more details of the weighting scheme). The aperture size is fixed on a physical scale and thus its apparent size on the sky varies with redshifts, at which we look for an overdensity of red galaxies. This radius is wide enough to include most of the galaxies in a candidate cluster, while it is small enough to detect weak signals from high-redshift clusters.

Using a fixed aperture to select galaxies for the red-sequence test is sufficient for our purposes as the probed mass range of systems

in the survey is narrow and 0.5 Mpc typically encompasses r_{500} of the system. An alternative choice of galaxy selection can be either X-ray extent or an estimate of r_{500} based on the redshift guess and X-ray properties of the system. The X-ray extent is determined by statistical significance of the detection and would introduce uneven demand on matching between galaxies and the X-ray source. Furthermore, for nearby objects the extent of the emission is predicted to go into the scales where confusion becomes important (2 arcmin for the depth of our survey), so the observed extent will be truncated. Using the fixed aperture, we can make a fair comparison of significance level of detection of overdensities at various redshifts.

3.3 Application of the red-sequence method

To probe if there is any overdensity of red galaxies at a given redshift z, we count galaxies around the model red sequence. We use a Gaussian weight when counting galaxies in a form of

$$\sum_i \exp\left\{-\left[\frac{colour_{i,\rm obs}-colour_{\rm model}(z)}{\sigma_{i,\rm obs}}\right]^2\right\} \times \exp\left\{-\left[\frac{mag_{i,\rm obs}-mag^*_{\rm model}(z)}{\sigma_{\rm mag}}\right]^2\right\} \times \exp\left[-\left(\frac{r_i}{\sigma_r}\right)^2\right], \quad (1)$$

where $colour_{i,\rm obs}$ and $mag_{i,\rm obs}$ are the colour and the magnitude of the ith observed galaxy, $\sigma_{i,\rm obs}$ is the observed colour error in $colour_{i,\rm obs}$, $colour_{\rm model}(z)$ is the model red-sequence colour at the magnitude of the observed galaxy, $mag^*_{\rm model}(z)$ is the characteristic magnitude based on the model, which is tuned to roughly reproduce the observed characteristic magnitudes, $\sigma_{\rm mag}$ is the smoothing parameter detailed below, r_i is the distance from the X-ray centre and σ_r is also a smoothing parameter as shown below. To account for systematic zero-point errors in observations and for systematic magnitude/colour errors in models, we take a minimum error in $\sigma_{i,\rm obs}$ of 0.1 mag. For example, if an object has $\sigma_{i,\rm obs} < 0.1$, we take $\sigma_{i,\rm obs} = 0.1$ for this object.

Since different colours are sensitive to red galaxies at different redshifts, we adopt the following combination of colours and magnitudes.

$0.0 < z < 0.5$: $B - i$ colour and i magnitude,
$0.5 < z < 1.0$: $R - z$ colour and z magnitude,
$1.0 < z < 1.5$: $i - K$ colour and K magnitude,
$1.5 < z < 2.5$: $z - 3.6$ μm colour and 3.6 μm magnitude.

In the SXDF, we have no U-band photometry, which is crucial for low-z red galaxies. Thus, our method is not very sensitive to clusters at $z < 0.3$ with estimated incompleteness in the cluster catalogue of ∼6 per cent.

The luminosity function of red galaxies varies with both richness of a cluster and redshift (Tanaka et al. 2005, 2007). To minimize the richness and redshift dependency of the red-sequence technique, we weight galaxies according to their luminosity. This is implemented in the second term of equation (1), by adding high weight to the detection of bright red galaxies, adjusted according to passive evolution model, and the smoothing parameter $\sigma_{\rm mag}$, which we set to a value of 2.

The third term in equation (1) takes into account the concentrations of galaxies. A galaxy at the centre of the cluster has heavier weight than that in the outskirts. The relative weight as a function of distance from the centre is controlled by the smoothing parameter σ_r. We take $\sigma_r = 1.0$ Mpc. This means that a galaxy at 0.5 Mpc from the centre (i.e. galaxy at the edge of the extraction aperture) has a $e^{-0.25} = 0.78$ weight relative to a galaxy at the centre. Altogether, we take into account the colour evolution and the magnitude evolution of the red sequence (first and second term, respectively), the concentration of galaxies (third term) and a density of red galaxies around the red sequence at any given redshift.

To quantify the significance of the overdensity of red galaxies at the position of a cluster candidate, we put an aperture of the same size at a random position in the SXDF and perform the same procedure 500 000 times. This gives an average number of red galaxies and its dispersion in the field at a given redshift. Then, the significance is evaluated as a relative overdensity of the cluster candidate to that of the field. A formal error of the red-sequence redshift is not straightforward to estimate since we use many parameters to derive the significance and the absolute significance changes with these parameters. To remedy this complexity, we simply take the full-width at half maximum of the significance peak as the error. In Table 1, we list the significance of the red sequence and the uncertainty of the redshift of the cluster.

4 SPECTROSCOPIC FOLLOW-UP

Since 2004 the $z < 1.3$ galaxy cluster candidates have been intensively followed up as a part of a SXDF VLA programme on the Very Large Telescope (VLT) and targeted Gemini proposals (Simpson et al. 2006). Geach et al. (2007) reported multi-object spectroscopy on four candidate X-ray galaxy groups around moderate-luminosity radio sources. van Breukelen et al. (2007, 2009) report some of the results of the Gemini programme. Other spectroscopic observations of the field are reported in Yamada et al. (2005), Smail et al. (2008) and Akiyama et al. (in preparation, 2dF/AAOmega). A total of 4 k spectra have been obtained thus far.

Using the identification of the cluster with a red-sequence method, we looked for spectroscopic redshifts of any of the red-sequence galaxies. Where there has been a consistent spectroscopic redshift found, we considered it as a refinement. Next, we searched for more spectroscopic redshifts in all galaxies matching the selected redshift to $0.005 \times (1 + z)$, which is twice a typical velocity dispersion. In addition, we have also looked for galaxy clustering at different redshifts, when data allowed, but found no outliers. In the cluster catalogue, we report both the spectroscopic redshift when available and a number of galaxies used to derive it, which can be used to assess the quality of the spectroscopic follow-up.

In Table 2, we list the coordinates and redshifts of the 144 galaxies assigned to the X-ray clusters. (The full version of this table is available in the online version of the paper – see Supporting Information.) In case the cluster has less than three spectroscopic members, this assignment is tentative.

5 A CATALOGUE OF IDENTIFIED X-RAY CLUSTERS

In this section, we describe our catalogue of 57 X-ray galaxy clusters detected in the SXDF/UDS field. In the catalogue (Table 1), we provide the cluster identification number (Column 1), RA and Dec. of the peak of the galaxy concentration identified with the extended X-ray source in Equinox J2000.0 (2–3), photometric redshift (4). In case there are spectroscopic redshift determinations for the cluster member galaxies, the median spectroscopic redshift is listed instead. The cluster flux in the 0.5–2 keV band is listed in Column 5 with the corresponding 1σ errors. The flux has units of

© 2010 The Authors. Journal compilation © 2010 RAS, MNRAS **403,** 2063–2076

Table 1. Catalogue of the SXDF X-ray selected galaxy groups.

ID	RA (Eq.2000)	Dec. (Eq.2000)	z	Flux (10^{-14} erg cm^{-2} s^{-1})	$L_{0.1-2.4\,\mathrm{keV}}$ (10^{42} erg s^{-1})	M_{200} (10^{13} M$_\odot$)	r_{200} (arcmin)	Flag	$N(z)$	Flux significance	Red sequence	redshift	median Photo-z	Ueda ID
(1)	(2)	(3)	(4)	(5)	(6)	(7)	(8)	(9)	(10)	(11)	(12)	(13)	(14)	(15)
SXDF01XGG	34.68284	−5.54973	0.378	1.11 ± 0.19	8.95 ± 1.54	7.30 ± 0.73	2.5	2	6	5.8	7.6	$0.29^{+0.05}_{-0.05}$	0.40	0876 0889
SXDF03XGG	34.33485	−5.48511	0.382	1.32 ± 0.33	10.94 ± 2.72	8.21 ± 1.17	2.5	1	5	4.0	2.3	$0.22^{+0.03}_{-0.06}$	0.35	
SXDF04XGG	34.47560	−5.45160	0.693	0.31 ± 0.09	11.69 ± 3.30	6.55 ± 1.05	1.5	2	3	3.4	8.7	$0.61^{+0.05}_{-0.06}$	0.70	0621
SXDF06XGG	34.73260	−5.47054	0.451	0.52 ± 0.12	6.52 ± 1.51	5.68 ± 0.76	2.0	1	4	4.3	8.5	$0.35^{+0.06}_{-0.03}$	0.45	0934
SXDF07XGG	34.60464	−5.41436	0.646	0.84 ± 0.13	24.67 ± 3.82	10.68 ± 0.96	1.9	1	6	6.5	8.4	$0.56^{+0.04}_{-0.07}$	0.65	0784
SXDF08XGG	34.36312	−5.41925	0.645	0.51 ± 0.08	15.49 ± 2.48	8.09 ± 0.75	1.7	2	3	6.4	5.3	$0.53^{+0.05}_{-0.04}$	0.65	
SXDF10XGG	34.19894	−4.55896	0.409	0.32 ± 0.11	3.21 ± 1.07	3.84 ± 0.72	1.9	3	2	2.9	1.5	$0.30^{+0.03}_{-0.01}$	0.40	
SXDF14XGG	34.49784	−4.63107	0.396	0.42 ± 0.13	3.88 ± 1.22	4.35 ± 0.78	2.0	5	2	3.2	3.3	$0.30^{+0.03}_{-0.10}$	0.35	
SXDF15XGG	34.23301	−4.65666	0.437	0.18 ± 0.05	2.06 ± 0.64	2.88 ± 0.51	1.6	1	1	3.6	4.7	$0.34^{+0.06}_{-0.12}$	0.40	
SXDF16XGG	34.35674	−4.65945	0.196	0.55 ± 0.13	0.92 ± 0.22	2.15 ± 0.30	2.8	1	3	4.2	1.9	$0.15^{+0.02}_{-0.02}$	0.25	0453
SXDF18XGG	34.53927	−4.67350	0.312	0.69 ± 0.19	3.39 ± 0.94	4.30 ± 0.68	2.4	2	2	3.6	2.8	$0.27^{+0.02}_{-0.04}$	0.30	
SXDF19XGG	34.35250	−4.68154	1.690	0.12 ± 0.04	51.12 ± 15.92	6.85 ± 1.21	0.9	3	0	3.0	2.4	$1.69^{+0.01}_{-0.10}$	1.73	
SXDF21XGG	34.56345	−4.75485	0.860	0.54 ± 0.21	32.32 ± 12.46	10.41 ± 2.25	1.5	3	0	2.6	2.8	$0.85^{+0.19}_{-0.06}$	0.90	
SXDF23XGG	34.40517	−4.79753	1.322	0.18 ± 0.05	38.35 ± 11.26	7.75 ± 1.29	1.1	3	1	3.6	2.6	$1.31^{+0.04}_{-0.06}$	1.40	
SXDF26XGG	34.28380	−4.84100	1.180	0.18 ± 0.06	27.55 ± 9.14	7.16 ± 1.34	1.1	1	1	3.0	5.1	$1.06^{+0.06}_{-0.03}$	1.05	
SXDF27XGG	34.94097	−4.81243	0.919	0.41 ± 0.08	30.52 ± 5.99	9.55 ± 1.08	1.4	1	1	5.1	9.0	$0.84^{+0.16}_{-0.15}$	0.90	
SXDF30XGG	34.39853	−4.83043	0.433	0.30 ± 0.06	3.35 ± 0.69	3.88 ± 0.46	1.8	1	2	5.0	4.1	$0.29^{+0.08}_{-0.04}$	0.40	
SXDF31XGG	34.35355	−4.84130	1.479	0.11 ± 0.03	34.91 ± 10.51	6.44 ± 1.10	1.0	3	1	3.7	2.4	$1.50^{+0.20}_{-0.01}$	1.50	
SXDF32XGG	34.80342	−4.84865	0.302	0.71 ± 0.16	3.22 ± 0.74	4.20 ± 0.55	2.4	3	2	4.4	2.7	$0.21^{+0.02}_{-0.02}$	0.33	
SXDF34XGG	34.42818	−4.86815	0.517	0.26 ± 0.07	4.50 ± 1.18	4.31 ± 0.65	1.6	1	3	3.7	3.2	$0.48^{+0.02}_{-0.03}$	0.50	0552
SXDF35XGG	34.49325	−4.86954	0.460	0.32 ± 0.05	4.25 ± 0.69	4.36 ± 0.41	1.8	2	0	6.4	5.3	$0.46^{+0.04}_{-0.04}$	0.45	0647
SXDF36XGG	34.93463	−4.88760	0.333	1.38 ± 0.14	8.00 ± 0.82	7.07 ± 0.43	2.7	1	10	9.9	3.6	$0.27^{+0.04}_{-0.07}$	0.35	1176
SXDF37XGG	34.80061	−4.89264	0.845	0.48 ± 0.08	27.61 ± 4.73	9.60 ± 0.96	1.5	1	1	6.0	4.1	$0.76^{+0.07}_{-0.05}$	0.85	
SXDF39XGG	34.14713	−4.91255	0.865	0.60 ± 0.11	35.99 ± 6.68	11.06 ± 1.19	1.6	3	1	5.5	4.2	$0.74^{+0.04}_{-0.04}$	0.78[a]	
SXDF40XGG	34.90565	−4.93738	0.140	0.78 ± 0.23	0.62 ± 0.19	1.77 ± 0.30	3.5	5	2	3.4	0.8	$0.16^{+0.01}_{-0.04}$	0.28[a]	
SXDF42XGG	34.84309	−4.97907	0.514	0.17 ± 0.06	3.04 ± 1.05	3.41 ± 0.66	1.5	1	3	2.8	1.0	$0.43^{+0.02}_{-0.02}$	0.45[a]	
SXDF43XGG	34.71921	−4.98955	0.514	0.17 ± 0.06	2.91 ± 1.08	3.32 ± 0.69	1.5	2	2	2.8	3.1	$0.40^{+0.05}_{-0.04}$	0.45	
SXDF44XGG	34.39690	−4.99191	0.425	0.18 ± 0.05	1.95 ± 0.60	2.82 ± 0.49	1.6	1	3	3.6	4.4	$0.35^{+0.03}_{-0.07}$	0.40	
SXDF45XGG	34.02448	−4.99410	0.309	0.41 ± 0.09	1.96 ± 0.41	3.10 ± 0.37	2.2	1	4	4.6	6.5	$0.18^{+0.08}_{-0.03}$	0.30	
SXDF46XGG	34.63196	−5.01653	0.875	0.87 ± 0.10	51.52 ± 5.66	13.61 ± 0.88	1.7	1	6	8.7	10.3	$0.77^{+0.12}_{-0.08}$	0.85	0829
SXDF47XGG	34.03081	−5.05366	0.348	0.59 ± 0.13	3.75 ± 0.84	4.43 ± 0.57	2.2	3	1	4.5	5.4	$0.21^{+0.03}_{-0.03}$	0.35[a]	0051
SXDF49XGG	34.53474	−5.07140	1.059	0.14 ± 0.04	16.74 ± 4.96	5.90 ± 0.99	1.1	2	3	3.5	4.7	$1.00^{+0.03}_{-0.01}$	1.05	
SXDF50XGG	34.87691	−5.05779	0.203	0.68 ± 0.15	1.22 ± 0.27	2.53 ± 0.32	2.9	3	3	4.5	2.4	$0.22^{+0.03}_{-0.02}$	0.35	
SXDF52XGG	34.81470	−5.08722	0.872	0.28 ± 0.07	18.80 ± 4.99	7.44 ± 1.13	1.4	3	2	4.0	3.0	$0.80^{+0.05}_{-0.22}$	0.85	

© 2010 The Authors. Journal compilation © 2010 RAS, MNRAS **403,** 2063–2076

Table 1 – *continued*

ID	RA (Eq.2000)	Dec.	z	Flux (10^{-14} erg cm^{-2} s^{-1})	$L_{0.1-2.4\,\mathrm{keV}}$ (10^{42} erg s^{-1})	M_{200} (10^{13} M$_\odot$)	r_{200} (arcmin)	Flag	$N(z)$	Flux significance	Red sequence	median Photo-z	Ueda ID
(1)	(2)	(3)	(4)	(5)	(6)	(7)	(8)	(9)	(10)	(11)	(12) redshift (13)	(14)	(15)
SXDF54XGG	34.16692	−5.08163	2.130	0.18 ± 0.07	117.33 ± 42.69	8.16 ± 1.67	0.9	3	0	2.6	2.7 $2.13^{+0.03}_{-0.03}$	2.20	
SXDF56XGG	34.97881	−5.11844	0.850	0.28 ± 0.10	17.14 ± 5.88	7.18 ± 1.39	1.4	3	0	2.8	5.1 $0.70^{+0.24}_{-0.05}$	0.85	
SXDF57XGG	34.94704	−5.13958	0.887	0.56 ± 0.11	36.45 ± 7.03	10.93 ± 1.22	1.5	1	2	5.1	6.5 $0.76^{+0.04}_{-0.11}$	0.85	
SXDF58XGG	34.01736	−5.13699	0.926	0.40 ± 0.15	29.96 ± 11.05	9.39 ± 1.95	1.4	3	2	2.7	1.9 $1.00^{+0.09}_{-0.10}$	1.00[a]	
SXDF59XGG	34.56808	−5.15206	1.810	0.11 ± 0.03	56.26 ± 15.62	6.62 ± 1.05	0.9	3	0	3.7	3.2 $1.81^{+0.08}_{-0.31}$	1.75	
SXDF60XGG	34.18937	−5.16353	1.410	0.30 ± 0.08	67.00 ± 16.91	10.07 ± 1.46	1.1	3	0	3.8	3.5 $1.41^{+0.03}_{-0.07}$	1.48	
SXDF63XGG	34.81285	−5.17151	1.590	0.21 ± 0.06	65.29 ± 18.32	8.58 ± 1.37	1.0	3	0	3.5	5.1 $1.59^{+0.11}_{-0.10}$	1.50	
SXDF64XGG	34.32375	−5.17140	1.030	0.14 ± 0.05	15.65 ± 5.69	5.81 ± 1.19	1.1	4	1	2.8	1.5 $0.85^{+0.06}_{-0.01}$	0.90	0396
SXDF66XGG	34.15841	−5.18202	0.548	0.33 ± 0.09	6.70 ± 1.84	5.32 ± 0.83	1.7	1	4	3.7	0.6 $0.60^{+0.02}_{-0.02}$	0.75[a]	
SXDF67XGG	34.63501	−5.19031	1.600	0.09 ± 0.04	36.61 ± 14.68	6.01 ± 1.35	0.9	3	0	2.2	4.7 $1.60^{+0.25}_{-0.10}$	1.60	
SXDF68XGG	34.85684	−5.20101	0.400	0.59 ± 0.15	5.63 ± 1.45	5.42 ± 0.80	2.1	5	0	3.9	2.5 $0.40^{+0.03}_{-0.03}$	0.45	
SXDF69XGG	34.39369	−5.22180	0.645	1.51 ± 0.11	42.00 ± 3.00	14.72 ± 0.62	2.1	1	9	13.7	14.3 $0.56^{+0.05}_{-0.06}$	0.65	0514
SXDF71XGG	34.27657	−5.22568	0.628	0.09 ± 0.04	3.07 ± 1.42	3.11 ± 0.80	1.3	1	2	2.2	2.5 $0.53^{+0.03}_{-0.03}$	0.65	
SXDF74XGG	34.39849	−5.29847	0.310	0.25 ± 0.09	1.22 ± 0.42	2.33 ± 0.45	2.0	3	3	2.8	4.3 $0.22^{+0.02}_{-0.03}$	0.35	
SXDF76XGG	34.74128	−5.32334	1.400	0.22 ± 0.09	50.76 ± 20.04	8.59 ± 1.90	1.1	3	0	2.4	9.5 $1.39^{+0.05}_{-0.06}$	1.40	
SXDF79XGG	34.24478	−4.55214	0.450	0.39 ± 0.09	4.80 ± 1.09	4.73 ± 0.62	1.9	3	0	4.3	2.5 $0.40^{+0.03}_{-0.05}$	0.45	0280
SXDF80XGG	34.61121	−4.53064	0.250	1.42 ± 0.52	4.29 ± 1.58	5.19 ± 1.07	3.0	5	1	2.7	0.0 –	–[a]	
SXDF83XGG	34.44151	−4.52622	0.491	0.46 ± 0.11	7.07 ± 1.66	5.77 ± 0.78	1.9	3	2	4.2	2.4 $0.39^{+0.06}_{-0.03}$	0.45	
SXDF84XGG	34.26719	−4.47831	0.663	0.34 ± 0.09	11.27 ± 2.98	6.58 ± 0.99	1.6	1	3	3.8	3.0 $0.64^{+0.04}_{-0.14}$	0.70	
SXDF85XGG	34.47978	−5.44818	0.250	0.41 ± 0.11	1.21 ± 0.34	2.43 ± 0.39	2.4	2	6	3.7	1.6 $0.15^{+0.05}_{-0.03}$	0.30	0621
SXDF87XGG	34.52729	−5.05699	1.402	0.17 ± 0.04	42.60 ± 9.42	7.72 ± 0.98	1.0	3	1	4.2	3.9 $1.36^{+0.08}_{-0.05}$	1.48	
SXDF88XGG	34.80176	−5.08379	0.195	0.41 ± 0.16	0.69 ± 0.28	1.80 ± 0.41	2.6	2	2	2.6	1.1 $0.15^{+0.03}_{-0.01}$	0.30	
SXDF89XGG	34.19625	−5.18181	0.249	0.19 ± 0.09	0.59 ± 0.28	1.58 ± 0.41	2.1	5	2	2.1	0.0 –	–	

[a] Stellar halo.

© 2010 The Authors. Journal compilation © 2010 RAS, MNRAS **403,** 2063–2076

Table 2. Spectroscopic redshifts of cluster member galaxies. This is a sample of the full table, which is available with the online version of the paper (see Supporting Information).

RA (Eq.2000) (1)	Dec. (2)	z (3)	Cluster ID (4)
34.672458	−5.534833	0.381	1
34.675250	−5.547528	0.381	1
34.678875	−5.580494	0.375	1
34.681125	−5.553822	0.375	1
34.690000	−5.545900	0.375	1
34.690667	−5.548917	0.383	1
34.315625	−5.488881	0.382	3
34.328500	−5.491192	0.381	3
34.332292	−5.502233	0.383	3
34.333792	−5.492828	0.381	3
34.359750	−5.507003	0.383	3
34.488667	−5.465550	0.694	4
34.470042	−5.438756	0.695	4
34.475771	−5.451581	0.690	4

10^{-14} erg cm^{-2} s^{-1}. The rest-frame luminosity in the 0.1–2.4 keV band in units of 10^{42} erg s^{-1} is given in (6). Column 7 lists the estimated total mass, M_{200}, computed following Rykoff et al. (2008) and assuming a standard evolution of scaling relations: $M_{200}E_z = f(L_X E_z^{-1})$. The corresponding R_{200} in arcmin is given in Column 8. Column 9 lists X-ray flag and the number of member galaxies inside R_{200}, $N(z)$ is given in Column 10. The errors provided on the derived properties are only statistical and do not include the intrinsic scatter in the L_X–M relation, which makes individual mass estimates uncertain by 0.2 dex (Vikhlinin et al. 2009). To provide insights on the reliability of both the source detection and the identification, in Column (11) we provide the significance of the X-ray flux estimate, and in Column (12) the significance of the red sequence. Column (13) shows the red-sequence redshift and its uncertainty. Column (14) provides the median photometric redshift of galaxies on the red sequence. Finally, Column (15) provides a reference to the extended source catalogue in Ueda et al. (2008).

Both flux estimates and the calculation of the properties of clusters are similar to the procedure outlined in Finoguenov et al. (2007). An X-ray quality flag (XFLAG) has been derived for the entire catalogue based on visual inspection. XFLAG = 1 is assigned to objects with high (in general > 6) significance of the X-ray flux estimate, and having a single optical counterpart. The next category of clusters (XFLAG = 2) is low significance detections, for which X-ray centring has a large uncertainty (up to 30 arcsec), hence a larger weight is given to the location of the optical counterpart. In addition, in the cases when a single X-ray source has been split into several sources, matching the optical counterpart, the assigned flag is set equal to 2 or larger. The clusters for which the photometric redshift of the optical or near-infrared counterpart is uncertain are flagged as XFLAG = 3, which is mostly a concern at $z > 1.2$. XFLAG = 4 indicates a presence of multiple optical counterparts, whose contribution to the observed X-ray emission is not possible to separate or rule out. Finally, the systems with potentially wrong assignment of an optical counterpart are marked as XFLAG = 5.

In Ueda et al. (2008), the results of the analysis of the same *XMM* data have been presented, identifying a total of 32 extended sources. The extended sources were identified by examining source extent over the point spread function assuming a Gaussian as the intrinsic image profile. For extended sources considered in this paper, we search for the sources from the Ueda et al. (2008) catalogue around the cluster central position within a radius of 32 arcsec, a typical size of significant extended emission. The positional errors (1σ) of the Ueda et al. (2008) sources are also taken into account in the matching. We recover 20 out of the 32 extended sources in Ueda et al. (2008) and identify 15 of them as clusters. In Table 1, we provide a match between our cluster catalogue and the extended sources in Ueda et al. (2008). The remaining differences can be understood as different sensitivities of the algorithm to extent of X-ray emission, which in our case is taken into account in the modelling of the survey.

5.1 Identification of X-ray jets and halo occupation statistics of radio-galaxies

Extensive inverse Compton X-ray emission from large radio galaxies has been detected above redshift 1, such as 3C 356 ($z = 1.12$; Simpson & Rawlings 2002), 3C 294 ($z = 1.786$; Fabian et al. 2003), 6C 0905+39 ($z = 1.833$; Erlund, Fabian & Blundell 2008) and 4C 23.56 ($z = 2.48$; Johnson et al. 2007). The flux of the emission depends on the energy density of the target photons, which in the case of the CMB rises as $(1 + z)^4$ so cancelling out the dimming expected from increased distance (Felten & Rees 1969; Schwartz 2002). Those studies predict a large number of extended sources detected in deep X-ray surveys, whose origin of the emission does not stem from the hot gas associated with potential wells of those systems, but is instead caused by the inverse Compton scattering of CMB photons on the relativistic electrons of an Mpc jet. However, there has not been a single survey that can quantify the effect.

In order to carry out this study, we use an expected match in the shape of the emission between the X-ray and radio source. We require a match in the orientation between X-ray and radio elongation to within 10°, therefore substantially reducing a chance correspondence between the X-ray and radio sources. We used the VLA survey of the field at 1.4 GHz to identify the radio sources (Simpson et al. 2006). The rms of the image is 12–20 μJ. There have been 14 complex morphology radio sources detected inside X-ray selected clusters in the SXDF, all shown in Fig. 3. Therefore, a positional and azimuthal match is subject to a chance alignment of 0.7 per cent, which can therefore be rejected with high confidence. With this method we have found three X-ray sources (IDs 25, 28 and 70) for which emission is entirely matched to a radio source. Three additional sources match substructure detected in the X-ray images (IDs 4, 39 and 69) and the original sources had to be split (introducing new sources 90, 91 and 92 assigned to X-ray jets) to ensure unbiased flux estimates of both components. In the case of cluster ID = 69 and X-ray jet ID = 92, the identification revealed different redshifts of the counterparts, therefore increasing the number of X-ray jets detected without detecting the cluster emission to four objects. This source has also been discussed in Geach et al. (2007) and Tu et al. (2009). All four objects also exhibit a match in spatial extent between radio and X-rays, which supports a physical link. The properties of the X-ray emission associated with the radio jets are summarized in Table 3. Column 1 lists object ID, Columns 2 and 3 list the coordinates of the centre of the X-ray emission, Column 4 reports the spectroscopic redshift of the radio galaxy, Column 5 reports the X-ray flux in units of 10^{-15} erg cm^{-2} s^{-1} and Column 6 displays the corresponding rest-frame luminosity in units of 10^{42} erg s^{-1}. We used the power-law model with photon index equal 2 in deriving the flux estimates and calculating the K-correction for X-rays and an $\alpha = 0.7$ index for the radio. Column (7) lists the radio counterpart in the catalogue of

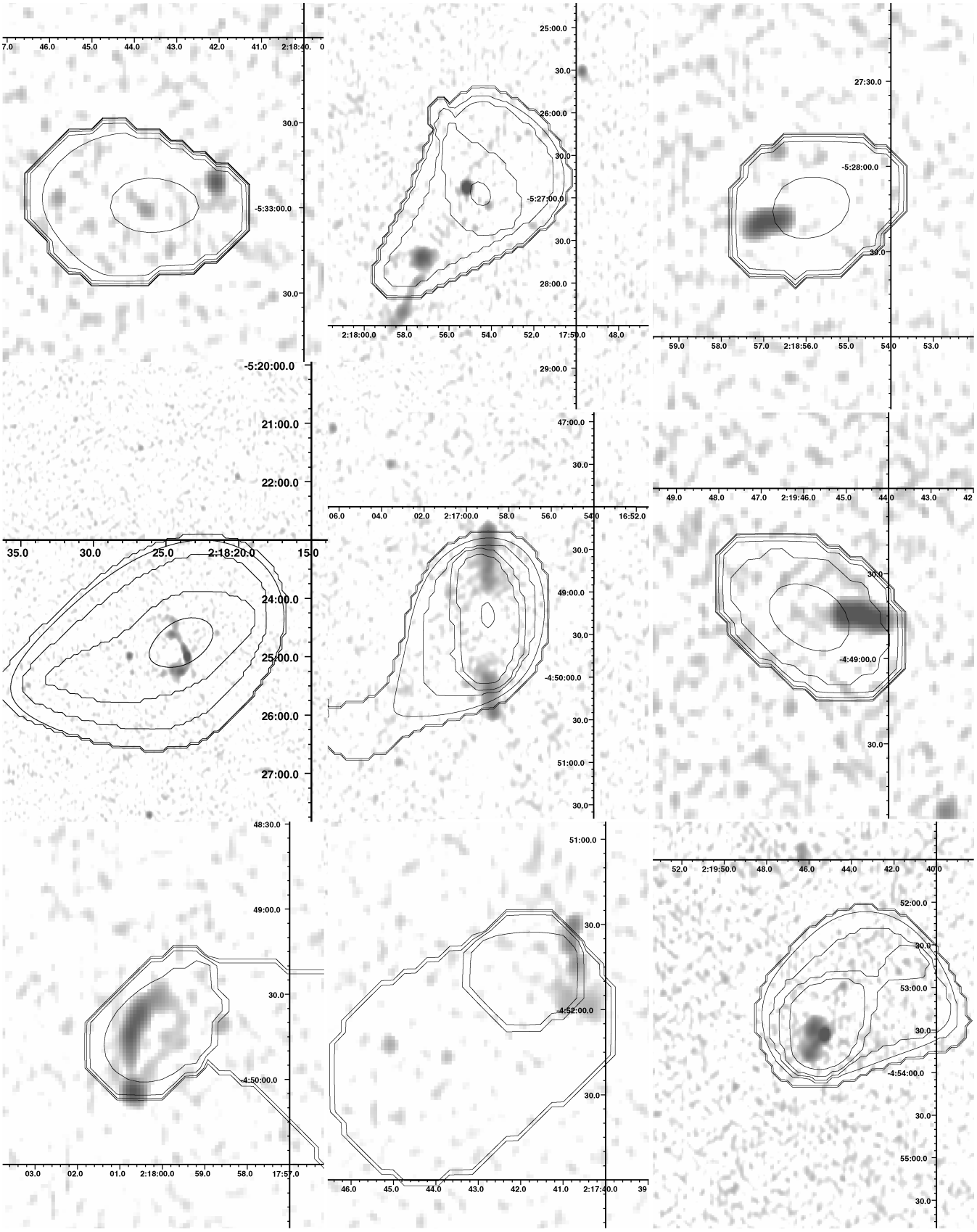

Figure 3. Comparison of complex radio sources with the extended X-ray emission in the SXDF. Images at 1.4 GHz frequency are overlaid with contours showing the wavelet reconstruction of extended X-ray emission on spatial scales of 32, 64 and 128 arcsec. From upper left to lower right, the cluster IDs are 1, 4, 6, 7, 25, 27, 28, 34 and 36. The coordinate grid is for the Equinox 2000. The astrometric differences will be of the order of 2 arcsec and do not matter for this comparison.

© 2010 The Authors. Journal compilation © 2010 RAS, MNRAS **403,** 2063–2076

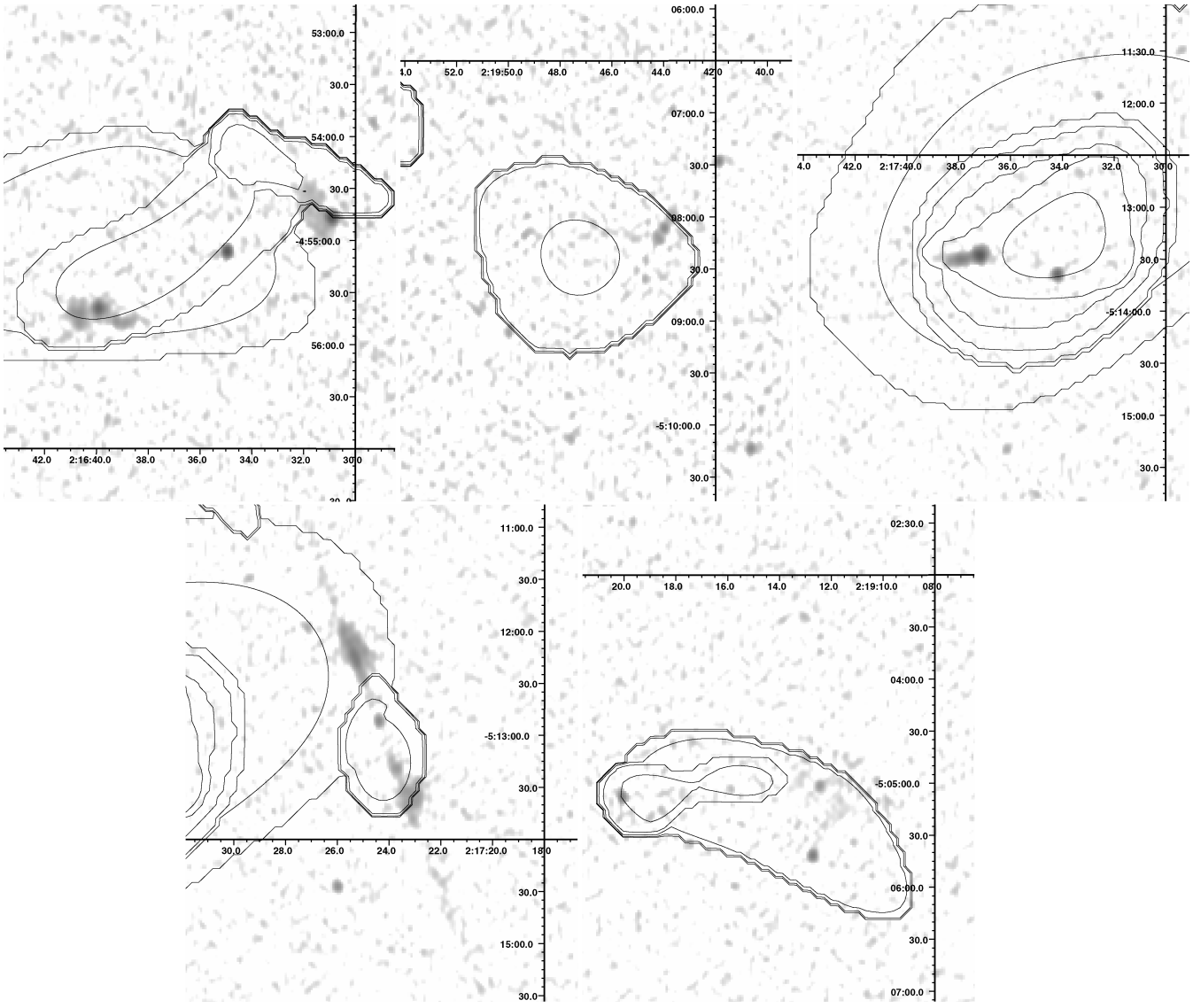

Figure 3 – *continued.* From upper left to lower right the cluster IDs are 39, 57, 69, 70 and 84.

Table 3. Properties of extended X-ray emission associated with radio jets.

ID host cluster (1)	RA (Eq.2000) (2)	Dec. (3)	z (4)	Flux (10^{-15} erg cm^{-2} s^{-1}) (5)	$L_{0.5-2\,\mathrm{keV}}$ (10^{42} erg s^{-1}) (6)	Simpson ID (7)	Flux (1.4 GHz, mJy) (8)	$L_{1.4\mathrm{GHz}}$ (10^{23} W Hz^{-1}) (9)	$L_x\nu_x/L_r\nu_r \times (1+z)^{-3.7}$ (10)
SXDF90XGG	34.47560	−5.45160	0.693	1.66 ± 0.50	3.6 ± 1.1	19	4.83	87 ± 1	4.2
SXDF25XGG	34.24682	−4.82231	1.179	6.85 ± 0.91	$54. \pm 7.1$	7	9.6	605 ± 2	3.6
SXDF28XGG	34.49991	−4.82799	0.192	1.24 ± 0.37	0.14 ± 0.04	20	4.6	4.4 ± 0.02	12.
SXDF91XGG	34.14713	−4.91255	0.865	0.74 ± 0.27	2.8 ± 1.0	12	6.59	200 ± 1	1.0[a]
SXDF92XGG	34.39369	−5.22180	0.645	0.80 ± 0.23	1.5 ± 0.4	33	2.37	36 ± 0.4	4.7
SXDF70XGG	34.35118	−5.21950	0.919	1.89 ± 0.34	8.2 ± 1.5	18	4.84	170 ± 1	3.1

[a]Only one radio lobe is used in the X-ray estimate.

Simpson et al. (2006), Column (8) reports the flux (F_r) at 1.4 GHz in mJy, Column (9) reports the rest-frame radio luminosity (L_r) at 1.4 GHz, calculated using the following formulae: $L_r = 4\pi D_L^2 F_r (1+z)^{(\alpha-1)}$. The luminosity distance (D_L) is calculated using the redshift listed in Column 4. The radio sources responsible for most of the inverse Compton (IC) emission are at the 10^{25} W Hz^{-1} level (the effect is detected from 20 per cent of all such radio sources), which are characterized by the volume abundance of $\sim 10^{-6}$ Mpc^{-3} dex^{-1} at redshifts near 1. Comparing to the theoretical model of Celotti & Fabian (2004), the IC effect detected in our survey is produced by the abundant sources at the faint end of the radio luminosity function they considered. This implies that the predictions in their fig. 3 need to be rescaled on the x-axis by a factor of 10. We can directly compute the required factor using our

X-ray and radio measurements, as reported in Column (9). Indeed the obtained ratio is larger than 1. We have already dropped the factor associated with the assumption of the evolution of the magnetic field (which lowers the inferred X-ray flux for a given radio flux), which adds another factor of 4, so on average a factor of 10 stronger production of X-rays compared to a conservative assumption in Celotti & Fabian (2004) is observed. All six radio sources listed in Table 3 are considered in detail as a part of the sample of Vardoulaki et al. (2008). At the same frequency, there is a good agreement with NRAO VLA Sky Survey (NVSS) measurements and only one source (radio ID = 7) has a steep spectrum (or much larger flux at lower frequencies compared to our estimate here). Thus, our conclusion on a factor of 10 stronger production of X-rays is neither an artefact nor a result of using a different frequency band compared to Celotti & Fabian (2004).

One of the X-ray jets is remarkably bright in X-rays (ID 25). It would be the most luminous cluster in the field, while an optical counterpart is barely detected. The X-ray jet is located near an X-ray detected group into which its host is probably accreting. The X-ray luminosity of the dominant group is an order of magnitude fainter than that of the X-ray jet. In Fig. 3, we present all 14 complex morphology radio sources located inside the extended X-ray emission.

In comparing the radio galaxy catalogue to the catalogue of X-ray clusters we note that a number of these sources match and the chances for the X-ray cluster to host a radio galaxy seem to increase with cluster mass. In order to characterize that we used our modelling of the survey to compute both the mass function of the full sample and the mass function of the X-ray clusters that host a radio galaxy. We have excluded the four cases where X-ray emission is caused by IC. In calculating the mass function, we take into account the volume of the survey towards each cluster mass. For radio galaxies, we select the luminosity-limited sample of $L_{1.4\,\mathrm{GHz}} > 5 \times 10^{23}\,\mathrm{W\,Hz^{-1}}$, which is valid to z of 1, given our flux limit of 100 μJy. We therefore restricted the cluster selection and volume computation to a redshift of 1. The limiting luminosity is located in the radio source population dominated by FRIs (core brightened), which therefore justifies our use of limits for a point source. Finally, since spectroscopic identification of the radio catalogue is not complete, we calculate two examples of matching: one is by taking the spectroscopically identified radio galaxies with redshifts matching that of the cluster and the other is by assuming that once the radio galaxy is located within the $0.2r_{200}$ it belongs to the cluster. There are 15 galaxies in total that fulfil this criterion, and after applying the radio luminosity threshold there are nine left, which we used to compute the marked mass function. Only one system has a photometric redshift for the radio galaxy, but the galaxy is also on the red sequence, suggesting that the association is real. The results are quantitatively similar and demonstrate in Fig. 4 that indeed the probability to observe a radio galaxy increases with mass of the halo. These results of a direct halo occupation distribution (HOD) determination for radio AGNs are in good agreement with clustering analysis of the 2dF-SDSS LRG and QSO Luminous Red Galaxy (2SLAQ LRG) survey (Wake et al. 2008), performed at redshifts near 0.6 and a similar selection of radio power.

5.2 Cluster counts

It is common to characterize a cluster survey by its area as a function of the limiting flux (which we do in Fig. 5) and present the results as a relation between a cumulative surface density of clusters above a given flux limit versus the flux value, the cluster $\log(N > S) - \log(S)$ (e.g. Rosati et al. 1998). The details of our calculation, which are shown in Fig. 6, are outlined in Finoguenov et al. (2007). In addition to the 57 identified sources, nine sources were located in the area with insufficient optical data due to either survey geometry or a presence of the bright star. In calculation of the upper limit on the $\log(N > S) - \log(S)$, we have added those sources using the typical flux extrapolation for our apertures of 1.2. Sources identified as X-ray counterparts of radio jets were not considered for $\log(N > S) - \log(S)$. 11 sources were located within the area of best photometric data, but still lacking identification, were not considered in the $\log(N > S) - \log(S)$. The computed uncertainties in $\log(N > S) - \log(S)$ are purely statistical. The comparison of the $\log(N > S) - \log(S)$ to COSMOS results of Finoguenov et al. (2007) reveals a

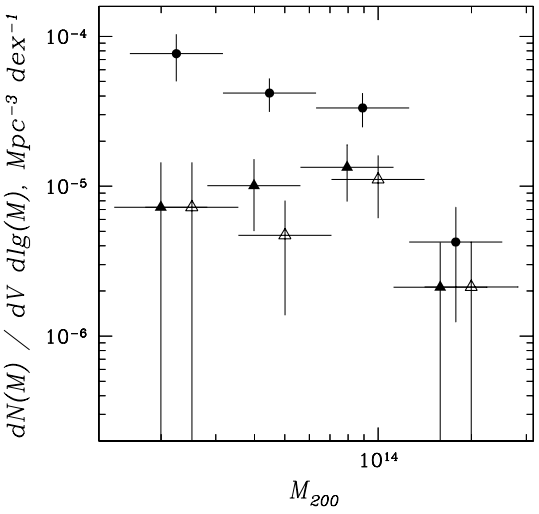

Figure 4. Mass function of $z < 1$ identified X-ray emitting haloes (solid circles with error bars) and those selected to have a radio galaxy from a luminosity-limited sample. Solid triangles with error bars show haloes with the spectroscopically confirmed radio galaxies within r_{200} and open triangles with error bars show matching within $0.2r_{200}$, but keeping the galaxies with consistent photometric redshift estimate but having no spectroscopic information.

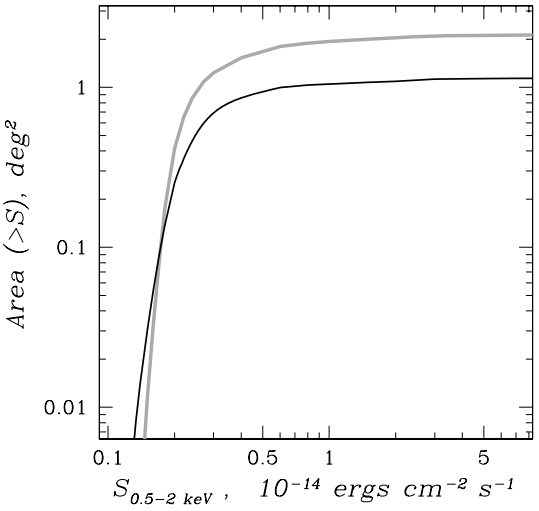

Figure 5. Survey area of the SXDF (black curve) as a function of the total source flux in the 0.5–2 keV band. The COSMOS flux-area curve corresponding to the results in Finoguenov et al. (2007) is shown as a grey line.

© 2010 The Authors. Journal compilation © 2010 RAS, MNRAS **403,** 2063–2076

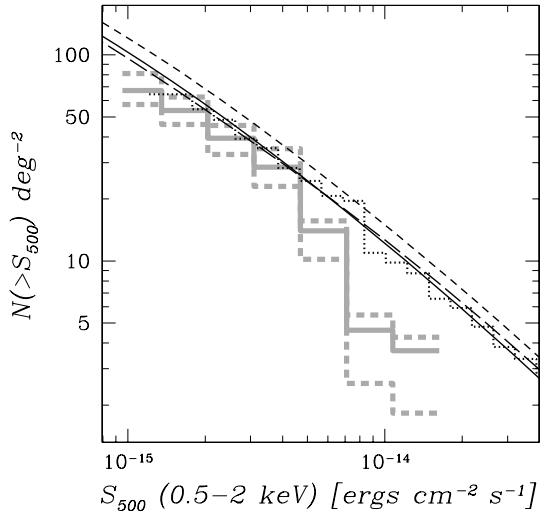

Figure 6. Cumulative cluster number counts [$\log(N > S) - \log(S)$] for the SXDF field. The solid grey histogram shows the data and dashed grey histograms denote the 68 per cent confidence interval. The dotted histogram shows a $\log(N > S) - \log(S)$ of the COSMOS survey. The long-dashed curve shows the prediction for no evolution in the luminosity function in Rosati et al. (2002), which provides a good fit to the data above 10^{-14} erg s^{-1} cm^{-2} flux. The dashed line shows the *WMAP*5 predictions for $\log(N > S) - \log(S)$ under our assumptions for scaling relations and their evolution excluding. The solid line has been produced to match observational predictions by adopting a 5 per cent reduction in σ_8.

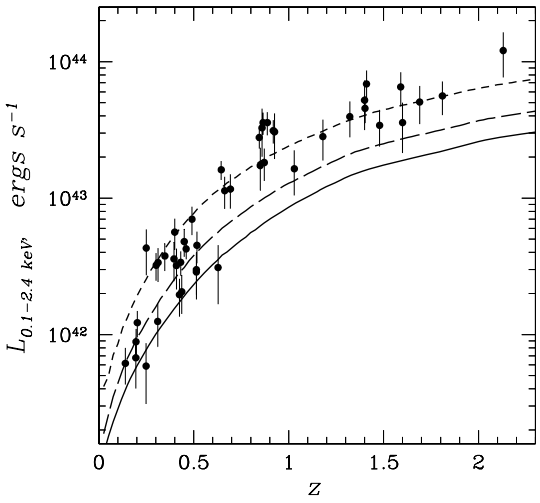

Figure 7. Illustration of the cluster luminosity probed as a function of cluster redshift in the SXDF. The filled circles represent the detected clusters with error bars based on the statistical errors in the flux measurements only. The short-dashed, long-dashed and solid black lines show the flux detection limits of −14.5 dex −14.8 dex and −15.0 dex associated with 90, 50 and 10 per cent of the total area, respectively.

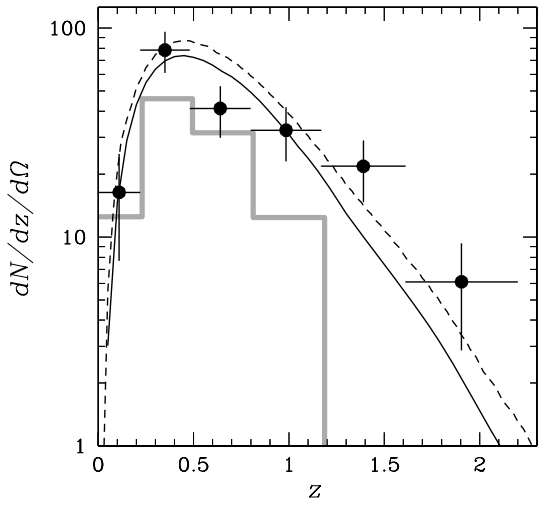

Figure 8. Differential redshift distribution ($dN/dz/d\Omega$ deg^{-2}) of 57 identified X-ray groups and clusters of galaxies in the SXDF (points with error bars). The thick grey histogram shows the spectroscopically confirmed systems. The short-dashed black curve shows the model prediction adopting *WMAP*5 cosmology. The solid line shows the *WMAP*5 prediction with a reduced by 5 per cent value of σ_8. Similar to Fig. 6, we are accounting for the incomplete identification by the 20 per cent upward correction for the data.

good agreement at low fluxes, while at fluxes exceeding 5×10^{-15} there is a lack of sources in the SXDF, compared to most previous surveys. The variation of statistics of bright sources is driven by the sample variance in such fields (Hu & Kravtsov 2003) and is very important for the field-to-field comparison (e.g. McCracken et al. 2007) on how clustering affects the conclusions regarding galaxy evolution. We present the previous modelling of the $\log(N > S) - \log(S)$ of Rosati et al. (2002), which describes well the cluster counts above 10^{-14} erg cm^{-2} s^{-1}. The short-dashed line is a result of combining the adopted scaling relations, *Wilkinson Microwave Anisotropy Probe 5 (WMAP5)* concordance cosmology (Komatsu et al. 2009) and a cosmological code of Peacock (2007). Since it clearly overpredicts the observed counts and previously published cluster counts, we considered the effect of excluding low-luminosity ($L_x < 10^{42}$ erg s^{-1}) or high-redshift clusters ($z > 1.2$) or both. None of these attempts was successful in providing a satisfactory solution. In order to match the observations, we adopted a 5 per cent lower value of σ_8, with a corresponding model prediction shown as a solid line. The role of the SXDF in implying a change in the cosmological parameters is however moderate, since the small size of the field causes large deviations at the bright end of the $\log(N > S) - \log(S)$.

5.3 Sample characteristics

In Fig. 7, we plot the observed characteristics of the SXDF cluster sample together with detection limits implied by both survey depth and our approach to search for clusters of galaxies.

In Fig. 8, we report the redshift distribution of the identified X-ray structures and attempt its modelling, assuming *WMAP*5 cosmology and using the adopted scaling relations and their evolution. Compared to a summary of scaling relations, presented in Finoguenov et al. (2007), we adopted direct $L_X - M$ calibrations of Rykoff et al. (2008), which match well with the results of COSMOS (Leauthaud et al. 2009). To compute the *K*-correction, we still need the *L*–*T* relation, for which we adopt

$$kT/\mathrm{keV} = 0.2 + 6 \times 10^{[lg(L_X/E_z/\mathrm{erg\,s^{-1}})-44.45)/2.1]} \quad (2)$$

and a fixed metallicity of 0.3 solar. The procedure for the flux extrapolation is the same as in Finoguenov et al. (2007). The *WMAP*5 concordance model prediction for the dN/dz is shown in Fig. 8 as a dashed curve, and our best-fitting model to $\log(N) - \log(S)$ data is shown as a solid curve. We show the results of our spectroscopic follow-up (grey histogram) and account for incompleteness in our red-sequence identification by increasing the counts by a

factor of 1.2, which accounts for the area with lack of optical data. Removing the contribution of low luminosity ($L_X < 10^{42}$ erg s^{-1}) systems produces a negligible result. The largest deviation between the data and the model is the lack of clusters in the 0.6–1. redshift range, which can also be seen in Fig. 7. The follow-up of the candidates (summarized as a grey histogram in Fig. 8) is quite complete at those redshifts, so it might be an effect of large-scale structure and will be investigated further through a comparison to other surveys like COSMOS. The number of missing clusters at those redshifts is around 10 similar to the deficit on $\log(N > S) - \log(S)$ at high fluxes. The number of our high-z candidates is consistent with the cosmological expectation.

5.4 X-ray luminosity function

The procedure of calculating the luminosity function is similar to COSMOS (Finoguenov et al. 2007).

In Fig. 9, we present the luminosity function of the SXDF clusters in the $0.2 < z < 1$ and $1 < z < 2.5$ redshift range. The choice of low redshift of 0.2 is due to incompleteness of the follow-up at low redshifts, and we also make an upward correction of the data by 1.2 accounting for incomplete coverage of the X-ray data by the optical data. The SXDF results for the $0.2 < z < 1$ compare well to the COSMOS results in the $0 < z < 1.2$ range, which are also shown in the figure (dashed line). In Fig. 9, we also show the prediction of our cosmological modelling and the assumed scaling relations. The model describes well both the luminosity function, and its redshift evolution.

We have tested the effects of log-normal scatter on the luminosity function with $\delta lg(L_X) = 0.2$ (Vikhlinin et al. 2009) and found them to be important only at $L_x > 10^{44}$ erg s^{-1}.

The sensitivity towards an assumption of a σ_8 value is not so large for low-mass systems, and in consistency with previous tests, we show the prediction of a 5 per cent reduced value of σ_8 in Fig. 9 (solid line). So, it is difficult to see if a particular part of the X-ray luminosity function (XLF) is causing a requirement for lowering the σ_8 value. Changing the Ω_m value would require a self-consistent recalibration of data, which is beyond the scope of this work, while the current data set is sensitive only to changes in Ω_m exceeding 10 per cent. Using galaxy groups, one can break the degeneracy between Ω_M and σ_8 present in fitting the cluster counts. The biggest remaining uncertainty is scatter in the scaling relations for galaxy groups, which is not well known.

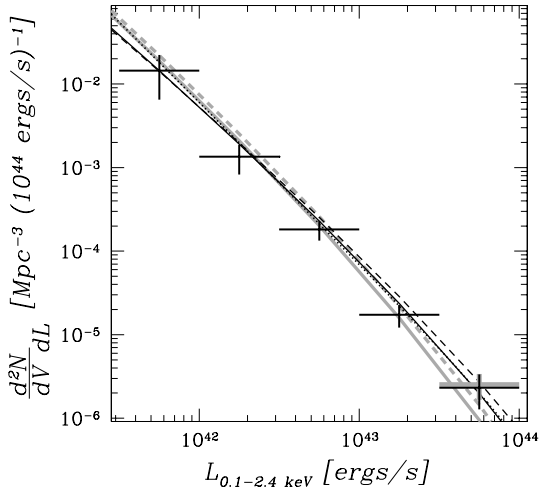

Figure 9. Luminosity function of clusters in the SXDF field. Black crosses indicate the data in the redshift range 0.2–1.0, and the grey point shows the data in the redshift range 1–2.5, which is the first measurement reported for $z > 1$. We apply the 20 per cent upward correction for incompleteness of cluster identification of the field. The dotted line shows the best fit to the COSMOS data over $0 < z < 1.2$ (Finoguenov et al. 2007). The dashed lines show the *WMAP*5 prediction for the luminosity function in the 0–1 (black) and 1–2.5 (grey) redshift range. Solid lines shows the change in the model due to a 5 per cent reduction in σ_8 value.

6 CONCLUSIONS

We have searched for extended X-ray emission in the SXDF and presented the catalogue of identified X-ray groups and clusters of galaxies. Our analysis of the extended X-ray emission in the SXDF revealed a new class of sources, associated with the inverse Compton emission from radio lobes. For extended objects identified as galaxy clusters, we derive the statistical properties of the survey and compare them to published results on COSMOS (Finoguenov et al. 2007) and the prediction of current best-fitting cosmology and cluster scaling relations. We considered $\log(N > S) - \log(S)$, dn/dz and XLF tests. The $\log(N > S) - \log(S)$ test showed that the SXDF lacks extended X-ray sources brighter than 5×10^{-15} erg cm^{-2} s^{-1}, compared to other surveys, which we attribute to sample variance. The XLF is in good agreement with COSMOS and is well modelled, but somewhat more uncertain due to incompleteness of the identification in the SXDF field. Comparing the *WMAP*5 cosmology together with the scaling relations for clusters to the cluster counts, we detect a sensitivity of the sample towards present uncertainty in the cosmological parameters and illustrate it by changing the value of σ_8 by 5 per cent to provide a best fit to our data and showing the change in the prediction for both $\log(N > S) - \log(S)$, dn/dz and XLF tests.

ACKNOWLEDGMENTS

In Germany, the *XMM–Newton* project is supported by the Bundesministerium fuer Wirtschaft und Technologie/Deutsches Zentrum fuer Luft-und Raumfahrt (BMWI/DLR, FKZ 50 OX 0001). A part of this work was supported by the Deutsches Zentrum für Luft– und Raumfahrt, DLR project numbers 50 OR 0207 and 50 OR 0405. AF acknowledges support from *Spitzer* UDS Legacy programme to UMBC. AF thanks Andy Fabian for useful discussions regarding the X-ray jets. AF thanks the University of Leicester for the hospitality during his frequent visits. The authors thank the referee for useful comments on the manuscript.

REFERENCES

Bauer F. E. et al., 2002, AJ, 123, 1163
Blakeslee J. P. et al., 2003, ApJ, 596, 143
Böhringer H. et al., 2002, ApJ, 566, 93
Borgani S., Guzzo L., 2001, Nat, 409, 39
Bower R. G., Lucey J. R., Ellis R. S., 1992, MNRAS, 254, 601
Bruzual G., Charlot S., 2003, MNRAS, 344, 1000
Burenin R. A., Vikhlinin A., Hornstrup A., Ebeling H., Quintana H., Mescheryakov A., 2007, ApJS, 172, 561
Celotti A., Fabian A. C., 2004, MNRAS, 353, 523
Cirasuolo M. et al., 2007, MNRAS, 380, 585
Erlund M. C., Fabian A. C., Blundell K. M., 2008, MNRAS, 386, 1774
Fabian A. C., Sanders J. S., Crawford C. S., Ettori S., 2003, MNRAS, 341, 729
Felten J. E., Rees M. J., 1969, Nat, 221, 924

Finoguenov A., Streblyanska A., Hasinger G., Hashimoto Y., Szokoly G., 2005, Adv. Space Res., 36, 710
Finoguenov A. et al., 2007, ApJS, 172, 182
Finoguenov A. et al., 2009, ApJ, 704, 564
Foucaud S. et al., 2007, MNRAS, 376, L20
Furusawa H. et al., 2008, ApJS, 176, 1
Geach J. E., Simpson C., Rawlings S., Read A. M., Watson M., 2007, MNRAS, 381, 1369
Giacconi R. et al., 2002, ApJS, 139, 369
Giodini S. et al., 2009, ApJ, 703, 982
Hu W., Kravtsov A. V., 2003, ApJ, 584, 702
Jansen F., Lumb D., Altieri B. et al., 2001, A&A, 365, L1
Johnson O., Almaini O., Best P. N., Dunlop J., 2007, MNRAS, 376, 151
Kirsch M. G. F. et al., 2004, Proc. SPIE, 5488, 103
Kodama T., Arimoto N., 1997, A&A, 320, 41
Komatsu E. et al., 2009, ApJS, 180, 330
Leauthaud A. et al., 2010, ApJ, 709, 97
Lidman C. et al., 2004, A&A, 416, 829
Lidman C. et al., 2008, A&A, 489, 981
Lonsdale C. J. et al., 2003, PASP, 115, 897
McCracken H. J. et al., 2007, ApJS, 172, 314
Mei S. et al., 2006, ApJ, 644, 759
Pacaud F. et al., 2007, MNRAS, 382, 1289
Peacock J. A., 2007, MNRAS, 379, 1067
Rosati P., della Ceca R., Norman C., Giacconi R., 1998, ApJ, 492, L21
Rosati P., Borgani S., Norman C., 2002, ARA&A, 40, 539
Rykoff E. S. et al., 2008, MNRAS, 387, L28
Saxton R. D. et al., 2005, 5 Years of Science with XMM-Newton. ESA, Noordwijk, p. 149
Schwartz D. A., 2002, ApJ, 569, L23
Silverman J. D. et al., 2009, ApJ, 695, 171
Simpson C., Rawlings S., 2002, MNRAS, 334, 511
Simpson C. et al., 2006, MNRAS, 372, 741
Smail I., Sharp R., Swinbank A. M., Akiyama M., Ueda Y., Foucaud S., Almaini O., Croom S., 2008, MNRAS, 389, 407
Smith R. K., Brickhouse N. S., Liedahl D. A., Raymond J. C., 2001, ApJ, 556, L91
Snowden S. L., Mushotzky R. F., Kuntz K. D., Davis D. S., 2008, A&A, 478, 615
Stanford S. A., Eisenhardt P. R., Dickinson M., 1998, ApJ, 492, 461
Strazzullo V. et al., 2006, A&A, 450, 909
Strüder L., Briel U. G., Dennerl K. et al., 2001, A&A, 365, L18
Tanaka M., Kodama T., Arimoto N., Okamura S., Umetsu K., Shimasaku K., Tanaka I., Yamada T., 2005, MNRAS, 362, 268
Tanaka M., Kodama T., Kajisawa M., Bower R., Demarco R., Finoguenov A., Lidman C., Rosati P., 2007, MNRAS, 377, 1206
Tanaka M. et al., 2008, A&A, 489, 571
Tu H. et al., 2009, A&A, 501, 475
Turner M. J. L. et al., 2001, A&A, 365, L27
Ueda Y. et al., 2008, ApJS, 179, 124
van Breukelen C. et al., 2007, MNRAS, 382, 971
van Breukelen C. et al., 2009, MNRAS, 395, 11
Vardoulaki E., Rawlings S., Simpson C., Bonfield D. G., Ivison R. J., Ibar E., 2008, MNRAS, 387, 505
Vikhlinin A. et al., 2009, ApJ, 692, 1033
Wake D. A., Croom S. M., Sadler E. M., Johnston H. M., 2008, MNRAS, 391, 1674
Watson M. G. et al., 2001, A&A, 365, L51
Yamada T. et al., 2005, ApJ, 634, 861
Zhang Y.-Y. et al., 2004, A&A, 413, 49

SUPPORTING INFORMATION

Additional Supporting Information may be found in the online version of this article:

Table 2. Spectroscopic redshifts of cluster member galaxies.

Please note: Wiley-Blackwell are not responsible for the content or functionality of any supporting materials supplied by the authors. Any queries (other than missing material) should be directed to the corresponding author for the article.

This paper has been typeset from a TEX/LATEX file prepared by the author.